Physica E 42 (2010) 1520–1530

Contents lists available at ScienceDirect

Physica E

journal homepage: www.elsevier.com/locate/physe

Properties of the Shannon entropy of arrays of elastic scatterers

W. Liu [a], J. Wan [a,*], M. Cahay [a], V. Gasparian [b], S. Bandyopadhyay [c]

[a] Department of Electrical and Computer Engineering, University of Cincinnati, Cincinnati, OH 45221, USA
[b] Department of Physics, California State University, Bakersfield, CA 93311, USA
[c] Department of Electrical and Computer Engineering, Virginia Commonwealth University, Richmond, VA 23284, USA

ARTICLE INFO

Article history:
Received 9 December 2009
Accepted 11 December 2009
Available online 21 December 2009

Keywords:
Effective spin
Shannon entropy
Elastic scatterers

ABSTRACT

Recently, we used an *effective spin* concept to expound the analogy between spin-based quantum information processing and phase coherent charge transport through an array of elastic scatterers. Here, we extend that analogy by calculating an effective Shannon entropy for such an array and examining its various properties. For single-moded transport, the Shannon entropy is given by $H_{bin}(|t|^2) = -|t|^2 \log_2 |t|^2 - |r|^2 \log_2 |r|^2$, where $|t|^2$ and $|r|^2$ are the transmission and reflection probabilities through the array of scatterers. A lower bound for $H_{bin}(|t|^2)$ is found starting with the entropic quantum uncertainty principle. An important result is that although evanescent channels (modes) have $|t|^2 = 1 - |r|^2 \to 0$, so that their own contribution to $H_{bin}(|t|^2) \to 0$, they nevertheless have a profound influence on the total $H_{bin}(|t|^2)$ of the array and its associated signal-to-noise ratio (SNR) since they renormalize the transmission probabilities of the propagating modes. This is reminiscent of the well-known fact that evanescent modes influence the conductance of a structure by renormalizing the transmission probabilities of the propagating modes.

The numerical values of $H_{bin}(|t|^2)$ and its SNR are strongly sensitive to the nature of the elastic scatterers, i.e., whether they are attractive (negative potential), repulsive (positive potential), or a combination of both. In samples with repulsive scatterers, the SNR can be tuned over a wide range by applying a potential through a gate to change the scattering potentials from repulsive to attractive by moving their energy levels with respect to the quasi-Fermi level in the sample. We also found that the mean free path of an electron traversing a random array of elastic scatterers is the length scale at which the sum of the cross-correlation coefficients of the effective spin components reaches a minimum. At that point, the sum of the effective Heisenberg and Zeeman Hamiltonians associated with effective spins describing the propagating channels, reaches a minimum. Hence the mean free path can be viewed as an order parameter for a phase transition.

1. Introduction

The effective spin concept is well known in the context of quantum optics and has been frequently used to describe and study spatial correlations between reflection and transmission amplitudes of polarized photon beams interacting with a combination of beam splitters, mirrors, and interferometers [1–3]. This spin concept was also used recently to examine entanglement between channels associated with propagating modes in mesoscopic systems [4,5]. Recently, we use the effective spin concept to examine the mathematical and physical analogy between phase coherent single-moded charge transport in mesoscopic systems and quantum operations on spin based qubits [6]. We used this analogy to reformulate well-known problems of tunneling through a delta scatterer, a resonant tunneling structure, a superlattice structure, and arrays of elastic scatterers, in terms of specific unitary operations (rotations) of a spinor on the Bloch sphere.

In this article, we extend the effective spin concept to address multi-moded charge transport in mesoscopic systems. We examine charge transport through two-dimensional random arrays of delta-scatterers from the ballistic to the strong localization regime and point out some interesting properties of the Shannon entropy content of these arrays. Some additional properties of the Shannon entropy of mesoscopic systems are analyzed to assess if random arrays of elastic scatterers can mimic quantum information processors. Somewhat expectedly, we found that evanescent modes affect the Shannon entropy of the array quite dramatically (even though their own individual contributions to the Shannon entropy is nearly zero), just as they affect the conductance of the array even though they themselves do not conduct and carry current [7–10]. Bagwell [7] has shown that evanescent states renormalize the coupling between propagating sates leading to a decrease (increase) in the transmission

* Corresponding author.
E-mail address: wanjunjun@yahoo.com (J. Wan).

1386-9477/$ - see front matter © 2010 Elsevier B.V. All rights reserved.
doi:10.1016/j.physe.2009.12.024

coefficients of the latter in the case of attractive (repulsive) scatterers. This results in the evanescent modes affecting both the Shannon entropy and the conductance of the array.

This article is organized as follows. In Section 2, the effective spin concept is introduced to describe coherent charge transport through an arbitrary one-dimensional sample (array of scatterers) as a sequence of unitary operations on an effective spin. Here, we assume that there is a single propagating mode (single-moded transport). Starting with the entropic quantum uncertainty principle, lower bounds for the Shannon binary entropy are then found. Section 3 presents numerical calculations of the Shannon entropy of random arrays of two-dimensional elastic scatterers, assuming multi-moded transport. Here, we show the importance of evanescent modes and how they affect the calculations. Additionally, we calculate the variance of the conductance, the variance of the Shannon entropy, and the signal-to-noise ratio of the entropy (defined as the ratio of its average over a large number of samples and its variance) as a function of sample length and the type of the impurities (repulsive, attractive, or a combination of both). The cross-correlation of the effective spin components are also calculated as a function of length. These coefficients are used to interpret the transition from ballistic transport, to weak and strong localization regimes in terms of effective Heisenberg and Zeeman Hamiltonians for the collection of effective spins associated with the propagating channels. Finally, Section 4 contains our conclusions.

2. The effective spin approach

We briefly revisit the effective spin concept. In tunneling problems, the transmission and reflection amplitudes of the tunneling wave are usually calculated by the so-called "scattering matrix approach" [11,12]. The scattering matrix relates the incoming (a^+, b^-) to outgoing wave amplitudes (b^+, a^-) on both sides of a scattering region (array of elastic scatterers), as shown in Fig. 1, such that

$$|\psi(OUT)\rangle = \begin{bmatrix} b^+ \\ a^- \end{bmatrix} = S \begin{bmatrix} a^+ \\ b^- \end{bmatrix} = \begin{bmatrix} t & r' \\ r & t' \end{bmatrix} \begin{bmatrix} a^+ \\ b^- \end{bmatrix} = S|\psi(IN)\rangle, \tag{1}$$

where S is the scattering matrix.

For single-moded transport, assuming an electron is incident from the left, we obtain

$$|\psi^l(IN)\rangle = \begin{bmatrix} 1 \\ 0 \end{bmatrix} \tag{2}$$

and

$$|\psi^l(OUT)\rangle = \begin{bmatrix} t \\ r \end{bmatrix}, \tag{3}$$

whereas, for an electron incident from the right, we have

$$|\psi^r(IN)\rangle = \begin{bmatrix} 0 \\ 1 \end{bmatrix} \tag{4}$$

and

$$|\psi^r(OUT)\rangle = \begin{bmatrix} r' \\ t' \end{bmatrix}. \tag{5}$$

The tunneling problem is completely characterized by the amplitudes (t, r) or (r', t') depending on the direction of incidence of the incoming electron.

Without any loss of generality, we can always think of the two-component column vector $|\psi(OUT)\rangle$ as a spinor, since it is normalized in the case of coherent transport. The normalization follows from the unitarity of the scattering matrix, i.e., $S^\dagger S = I$. Furthermore, the spinor $|\psi(OUT)\rangle$ can be thought as the output of a one-qubit quantum gate whose input is the spinor $|\psi(IN)\rangle = (1,0)^\dagger$ or $(0,1)^\dagger$ (where † stands for Hermitian conjugate) depending on the direction of propagation of the incident electron. The 2×2 unitary matrix linking the spinors $|\psi(IN)\rangle$ and $|\psi(OUT)\rangle$ can therefore be viewed as the matrix characterizing rotation of a qubit whose initial state was $|\psi(IN)\rangle$ and whose final state becomes $|\psi(OUT)\rangle$. This matrix is also the scattering matrix describing the tunneling problem.

2.1. The effective spin components and their physical interpretation

We refer to the (2×1) column vector $|\psi^l(OUT)\rangle$ in Eq. (3) as the *effective spin* whose components characterize completely the scattering amplitudes of the tunneling electron. For an arbitrary potential energy profile $E_c(x)$ describing the potential landscape of an array of elastic scatterers, the amplitude $|\psi^l(OUT)\rangle$ can be found by successively cascading scattering matrices associated

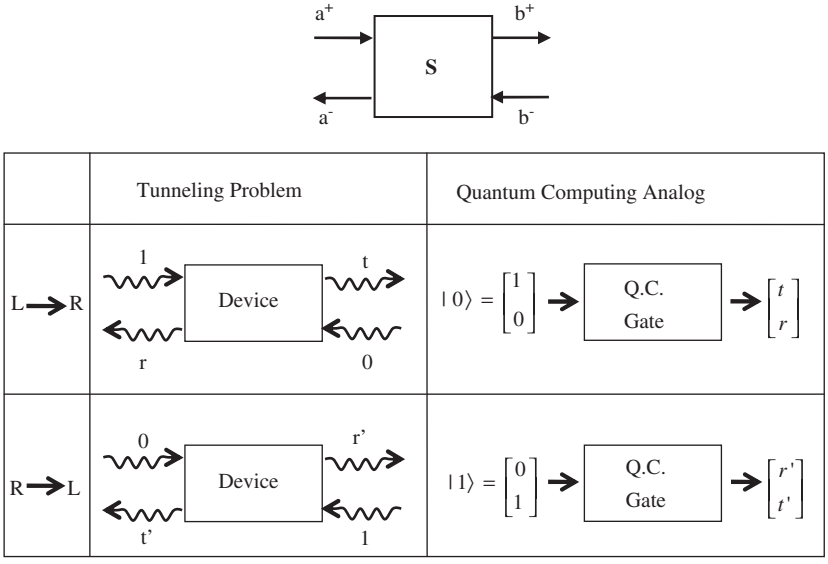

Fig. 1. The tunneling problem and its quantum computing gate equivalent. The scattering matrix associated with a device relates the incoming (a^+, b^-) to the outgoing (a^-, b^+) wave amplitudes. It can be viewed as the matrix representing the rotation of a qubit from the initial state $|\psi(IN)\rangle$ to the final state $|\psi(OUT)\rangle$.

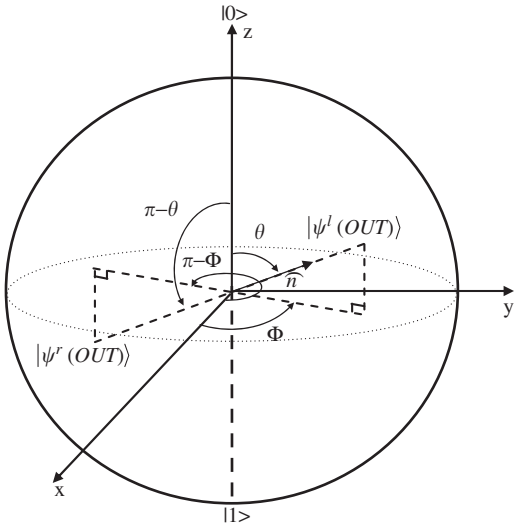

Fig. 2. Bloch sphere representation of the effective spin (qubit) $|\psi(OUT)\rangle$. The radius of the sphere is equal to 1.

with "subsections" within each of which $E_c(x)$ is approximated by constant values E_{c1}, E_{c2}, $E_{c3}, \ldots, E_{cn}$ [11,12]. The evolution of the pure state $|\psi^l(OUT)\rangle$ after crossing a number of subsections can be represented using the Bloch sphere concept in which the spinor is parameterized as follows [13,14]:

$$|\psi^l(OUT)\rangle = e^{i\gamma}\left[\cos\frac{\theta}{2}|0\rangle + \sin\frac{\theta}{2}e^{i\varphi}|1\rangle\right], \tag{6}$$

where γ is an arbitrary phase factor and the angles (φ, θ) are the azimuthal and polar angles, as shown in Fig. 2.

In Eq. (6), $|0\rangle$ and $|1\rangle$ are the (2×1) column vectors $(1,0)^\dagger$ and $(0,1)^\dagger$ respectively, associated with the north and south poles of the Bloch sphere. They are mutually orthogonal, i.e., their inner product $<0|1>=0$ [13].

To complete the effective spin picture, we consider the following 2×2 matrix [15]:

$$\rho = |\psi^l(OUT)\rangle\langle\psi^l(OUT)| = \begin{pmatrix} t \\ r \end{pmatrix}(t^* r^*) = \begin{pmatrix} |t|^2 & tr^* \\ rt^* & |r|^2 \end{pmatrix}. \tag{7}$$

Using this density matrix and the Pauli spin matrices (σ_x, σ_y, σ_z), the effective "spin components" associated with the spinor $|\psi^l(OUT)\rangle$ are given by

$$\langle S_x\rangle = \frac{\hbar}{2}\mathrm{Tr}(\rho\sigma_x) = \frac{\hbar}{2}(tr^* + rt^*) = \hbar\,\mathrm{Re}(rt^*) = \hbar\,\mathrm{Re}(r^*t), \tag{8}$$

$$\langle S_y\rangle = \frac{\hbar}{2}\mathrm{Tr}(\rho\sigma_y) = \frac{\hbar}{2}i(tr^* - rt^*) = \hbar\,\mathrm{Im}(rt^*) = -\hbar\,\mathrm{Im}(r^*t), \tag{9}$$

and

$$\langle S_z\rangle = \frac{\hbar}{2}\mathrm{Tr}(\rho\sigma_z) = \frac{\hbar}{2}(|t|^2 - |r|^2) = \frac{\hbar}{2}(1-2|r|^2) = \frac{\hbar}{2}(2|t|^2 - 1). \tag{10}$$

For an electron incident from the right, $|\psi^r(IN)\rangle = |1\rangle$, and the density matrix $\rho' (= |\psi^r(OUT)\rangle\langle\psi^r(OUT)|)$ is such that $\rho' = 1-\rho$, where ρ is given by Eq. (7) and the components $\langle S_x\rangle$, $\langle S_y\rangle$ and $\langle S_z\rangle$ are just the negative of the values in Eqs. (8)–(10). Therefore, the two spinors corresponding to $|\psi^l(OUT)\rangle$ and $|\psi^r(OUT)\rangle$ are mirror images of each other, corresponding to a reflection through the origin of the Bloch sphere. This means that $|\psi^l(OUT)\rangle$ and $|\psi^r(OUT)\rangle$ are orthogonal, which they must be because the scattering matrix is unitary. Furthermore, using Eqs. (8)–(10), we get

$$\langle S_x\rangle^2 + \langle S_y\rangle^2 + \langle S_z\rangle^2 = \hbar^2/4. \tag{11}$$

Since $(\langle S_x\rangle, \langle S_y\rangle, \langle S_z\rangle)$ are proportional to the components of the spinor $|\psi(OUT)\rangle$ on the Bloch sphere, Eq. (11) simply states that the spinor stays on the Bloch sphere during cascading of scattering matrices. This is expected for the case of coherent transport. Furthermore, since $\langle S_x^2\rangle = \langle S_y^2\rangle = \langle S_z^2\rangle = \hbar^2/4\,\mathrm{Tr}\,\rho = \hbar^2/4$, the square of the variance of the effective spin components $\Delta_x^2 = \langle S_x^2\rangle - \langle S_x\rangle^2$ and $\Delta_y^2 = \langle S_y^2\rangle - \langle S_y\rangle^2$ can easily be calculated as

$$\Delta_x^2 + \Delta_y^2 = \frac{\hbar^2}{2}(1-2|r|^2|t|^2). \tag{12}$$

Since $|r|^2|t|^2$ has a maximum when $|r| = |t| = 1/\sqrt{2}$, $\Delta_x^2 + \Delta_y^2$ reaches a minimum of $\hbar^2/4$ when the spinor is in the equatorial plane of the Bloch sphere.

2.2. Physical interpretation of the effective components

The effective spin components $\langle S_x\rangle$ and $\langle S_y\rangle$ appear in the calculation of many physical quantities describing charge transport through mesoscopic systems. As an example consider an Aharanov–Bohm interferometer shown in Fig. 3 for which there is a single propagating mode in both leads and also in the upper and lower arms of the interferometer. Neglecting the effects of multiple reflections and assuming the incident wave can only be transmitted in the upper branch (with probability amplitude t) or reflected in the lower branch (with probability amplitude r), the total amplitude of the wave at point P, is given by

$$\psi_P = re^{ik_l L} + te^{ik_u L}, \tag{13}$$

where k_l and k_u are the wavevectors of the propagating mode in the lower and upper branches of the ring, respectively. The length of each arm is assumed to be the same but the following argument could be extended to interferometers with different arm lengths as well. The probability density at point P is therefore given by

$$|\psi_P|^2 = |r|^2 + |t|^2 + r^* t e^{i(k_u - k_l)L} + rt^* e^{i(k_l - k_u)L}, \tag{14}$$

where $k_d = k_u - k_l$.

Since $|r|^2 + |t|^2 = 1$, we get

$$|\psi_P|^2 = 1 + 2\,\mathrm{Re}(rt^*)\cos k_d L + 2\,\mathrm{Im}(rt^*)\sin k_d L. \tag{15}$$

Hence, the interference pattern at the point of exit contains two terms whose amplitudes are proportional to the effective spin

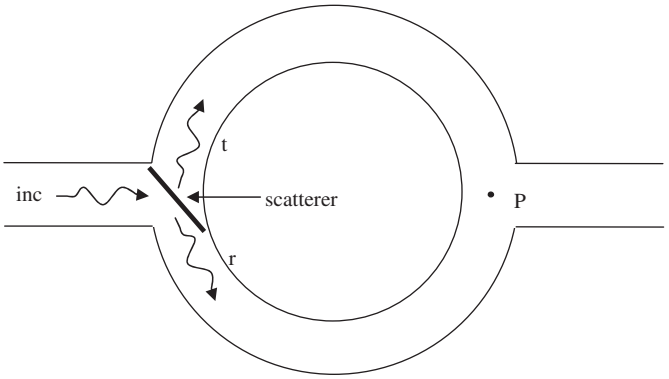

Fig. 3. In a single-moded Aharamov–Bohm interferometer, a wave incident from the left on a scattering region located at the leftmost 3-way splitter is transmitted with amplitude t in the upper arm and amplitude r in the lower arm. If no reflection in the left lead is allowed, $|t|^2 + |r|^2 = 1$. The interference pattern at point P at the rightmost 3-way splitter has components with amplitudes proportional to the effective spin components associative to the effective spinor describing the scattering problem.

components $\langle S_x \rangle$ and $\langle S_y \rangle$. Eq. (15) can be rewritten as follows:

$$|\psi_P(k_dL)|^2 = 1 + \frac{2}{\hbar}\langle S_x \rangle \cos k_dL + \frac{2}{\hbar}\langle S_y \rangle \sin k_dL \tag{16}$$

or equivalently,

$$|\psi_P(k_dL)|^2 = 1 + \mathrm{Tr}(\rho\sigma_x)\cos k_dL + \mathrm{Tr}(\rho\sigma_y)\cos k_dL. \tag{17}$$

Furthermore, the unitarity of the scattering matrix also leads to

$$\langle S_x \rangle^2 + \langle S_y \rangle^2 = \hbar^2|t|^2(1-|t|^2). \tag{18}$$

Eq. (16) shows that the projection of the spinor in the equatorial plane of the Bloch sphere reaches a maximum when $|t| = |r| = 1/\sqrt{2}$. Actually, $\langle S_x \rangle^2 + \langle S_y \rangle^2$ is proportional to $|t|^2(1-|t|^2)$, i.e., the low frequency shot noise power for the tunneling electron [16].

The angles $(\gamma, \theta, \varphi)$ appearing in the generic expression of the spinor (or qubit) in Eq. (6) can be expressed in terms of the phases and magnitudes of the reflection and transmission coefficients:

$$|\psi^I(OUT)\rangle = \begin{bmatrix} t \\ r \end{bmatrix} = \begin{bmatrix} |t|e^{i\phi_T} \\ |r|e^{i\phi_R} \end{bmatrix} = e^{i\phi_T}\begin{bmatrix} |t| \\ |r|e^{i(\phi_R-\phi_T)} \end{bmatrix}, \tag{19}$$

where ϕ_R and ϕ_T are the phases of the reflection and transmission amplitudes, respectively.

We get

$$\gamma = \phi_T \tag{20}$$

and

$$\phi = \phi_R - \phi_T. \tag{21}$$

Furthermore,

$$|t| = \cos\frac{\theta}{2}, \tag{22}$$

$$|r| = \sin\frac{\theta}{2} = \sqrt{1-|t|^2} \tag{23}$$

and therefore,

$$\frac{\theta}{2} = \tan^{-1}\left(\frac{|r|}{|t|}\right). \tag{24}$$

Eqs. (8)–(10) are therefore equivalent to

$$\langle S_x \rangle = \frac{\hbar}{2}\sin\theta\cos\varphi, \tag{25}$$

$$\langle S_y \rangle = \frac{\hbar}{2}\sin\theta\sin\varphi \tag{26}$$

and

$$\langle S_z \rangle = \frac{\hbar}{2}\cos\theta, \tag{27}$$

Eqs. (8) and (9) clearly show that the averages $\langle S_x \rangle$ and $\langle S_y \rangle$ contain more information than the sample conductance alone. The latter depends only on the magnitude of transmission $|t|$ or reflection $|r|$ in the Landauer picture [17–20], whereas $\langle S_x \rangle$ and $\langle S_y \rangle$ depend on the phase relationship between t and r as well. The phase relationship is a strong function of the energy of the incident electron. At non zero temperature, there will be a thermal spread in the energy of the incident electron which will lead to a rapid wash out with temperature of the components $\langle S_x \rangle$ and $\langle S_y \rangle$, i.e., the off-diagonal components of the density matrix ρ. Note that while $\langle S_x \rangle$ and $\langle S_y \rangle$ depend on the off-diagonal components of the density matrix and are very energy sensitive, $\langle S_z \rangle$ depends only on the diagonal components of the density matrix and is much less energy sensitive.

2.3. The Shannon entropy and the entropic quantum uncertainty principle

For a single-moded structure, the outcome of a measurement of the scattered amplitudes will lead to the probabilities $|r|^2$ and $|t|^2$. The information content of this probability distribution is given by the binary entropy [13]

$$H_{bin}(|t|^2) = -|t|^2\log_2|t|^2 - |r|^2\log_2|r|^2, \tag{28}$$

which is a special case of the Shannon entropy for the case of a random variable with only two outcomes, $|r|^2$ or $|t|^2$.

Eq. (26) shows that $H_{bin}(|t|^2) = H_{bin}(|r|^2)$, since $|r|^2 + |t|^2 = 1$. Therefore, $H_{bin}(|t|^2)$ reaches its maximum value of 1 when $|r|^2 = |t|^2 = 1/2$. At this point, the conductance of the sample is equal to e^2/h. This occurs when the sample length is equal to the elastic mean free path of the scattering region. Stated otherwise, the information content in $|\psi(OUT)\rangle$ is maximum when the latter lies in the equatorial plane of the Bloch sphere. When this occurs, the square of the norm of the effective spin, i.e., $\langle S_x \rangle^2 + \langle S_y \rangle^2$ is proportional to $|t|^2(1-|t|^2)$. The latter is proportional to the shot noise power spectrum of the scattering region and reaches a maximum value of 0.25 when $|r|^2 = |t|^2 = 1/2$.

Next, we derive a lower bound for $H_{bin}(|t|^2)$ starting with the entropic quantum uncertainty principle [13]. The latter states that, if $C = \sum_c c|c\rangle\langle c|$ and $D = \sum_d d|d\rangle\langle d|$ are the spectral decompositions for C and D, and $f(C,D) = \max_{(c,d)}|\langle c|d\rangle|$ is the maximum fidelity between any two eigenvectors of $|c\rangle$ and $|d\rangle$, then

$$H(C) + H(D) \geq 2\log_2\left[\frac{1}{f(C,D)}\right], \tag{29}$$

where

$$H(C) + H(D) = -\sum_{(c,d)} p(c)q(d)\log_2(p(c)q(d)) \tag{30}$$

and $p(c)q(d) = |\langle c|\psi\rangle\langle\psi|d\rangle|^2$.

Here, $|\psi\rangle$ is the quantum state of the system, $p(c)$ is the probability distribution associated with a measurement of C with Shannon entropy $H(C)$, and $q(d)$ the probability distribution associated with a measurement of D with Shannon entropy $H(D)$.

If we use the operator $C = \sigma_x$ and $D = \sigma_z$, then $f(\sigma_x, \sigma_z) = 1/\sqrt{2}$. The inequality (29), where the pure state of the quantum system $|\psi\rangle$ is the effective spin state $|\psi(OUT)\rangle$, leads to

$$g(\langle S_x \rangle) \leq H_{bin}(|t|^2), \tag{31}$$

where

$$g(\langle S_x \rangle) = \frac{1}{2}\left(1 + \frac{2}{\hbar}\langle S_x \rangle\right)\log_2\left[1 + \frac{2}{\hbar}\langle S_x \rangle\right] + \frac{1}{2}\left(1 - \frac{2}{\hbar}\langle S_x \rangle\right)\log_2\left[1 - \frac{2}{\hbar}\langle S_x \rangle\right]. \tag{32}$$

Similarly, for $C = \sigma_y$ and $D = \sigma_z$ in the inequality (29), we get

$$g(\langle S_y \rangle) \leq H_{bin}(|t|^2). \tag{33}$$

The two inequalities (31) and (33) can be replaced by the single inequality

$$\max(g(\langle S_x \rangle), g(\langle S_y \rangle)) \leq H_{bin}(|t|^2) \tag{34}$$

producing a lower bound for the binary entropy.

The inequalities (31) and (33) can be recast in a more physically appealing form. Using Eq. (16), we get

$$|\psi_P(2n\pi)|^2 = 1+\frac{2}{\hbar}\langle S_x\rangle, \tag{35}$$

$$\left|\psi_P\left((2n+1)\frac{\pi}{2}\right)\right|^2 = 1+\frac{2}{\hbar}\langle S_y\rangle, \tag{36}$$

$$|\psi_P((2n+1)\pi)|^2 = 1-\frac{2}{\hbar}\langle S_x\rangle, \tag{37}$$

and

$$\left|\psi_P\left((2n+1)\frac{3\pi}{2}\right)\right|^2 = 1-\frac{2}{\hbar}\langle S_y\rangle. \tag{38}$$

Using those last four equations, the inequality (31) can be recast as follows:

$$\tfrac{1}{2}[|\psi_P(2n\pi)|^2\log_2|\psi_P(2n\pi)|^2+|\psi_P((2n+1)\pi)|^2 \log_2|\psi_P((2n+1)\pi)|^2] \le H_{bin}(|t|^2). \tag{39}$$

Similarly, the inequality (33) becomes

$$\frac{1}{2}\left[\left|\psi_P\left((2n+1)\frac{\pi}{2}\right)\right|^2\log_2\left|\psi_P\left((2n+1)\frac{\pi}{2}\right)\right|^2 + \left|\psi_P\left((2n+1)\frac{3\pi}{2}\right)\right|^2\log_2\left|\psi_P\left((2n+1)\frac{3\pi}{2}\right)\right|^2\right] \le H_{bin}(|t|^2). \tag{40}$$

In the interferometer shown in Fig. 3, a measurement of the intensity of the interfering beam at point P, while adjusting the phase shift in both arms of the interferometer with independent gates, can provide lower bounds for the Shannon entropy of an array of elastic scatterers.

Finally, another relation between the effective spin components $\langle S_x\rangle$ and $\langle S_y\rangle$ can be found starting with the inequality (29) with $C=\sigma_x$ and $D=\sigma_y$. In that case, we obtain

$$h(\langle S_x\rangle,\langle S_y\rangle)\le 4, \tag{41}$$

where $h(\langle S_x\rangle,\langle S_y\rangle)$ is equal to

$$\begin{aligned}&(1+C_{+,-}(\langle S_x\rangle,\langle S_y\rangle))\log_2(1+C_{+,-}(\langle S_x\rangle,\langle S_y\rangle))\\ &+(1+C_{+,+}(\langle S_x\rangle,\langle S_y\rangle))\log_2(1+C_{+,+}(\langle S_x\rangle,\langle S_y\rangle))\\ &+(1+C_{-,-}(\langle S_x\rangle,\langle S_y\rangle))\log_2(1+C_{-,-}(\langle S_x\rangle,\langle S_y\rangle))\\ &+(1+C_{-,+}(\langle S_x\rangle,\langle S_y\rangle))\log_2(1+C_{-,+}(\langle S_x\rangle,\langle S_y\rangle)),\end{aligned}$$

where

$$C_{+,-}(\langle S_x\rangle,\langle S_y\rangle)=\frac{2}{\hbar}\left[\langle S_x\rangle-\langle S_y\rangle-\frac{2}{\hbar}\langle S_x\rangle\langle S_y\rangle\right], \tag{42}$$

$$C_{+,+}(\langle S_x\rangle,\langle S_y\rangle)=\frac{2}{\hbar}\left[\langle S_x\rangle+\langle S_y\rangle+\frac{2}{\hbar}\langle S_x\rangle\langle S_y\rangle\right], \tag{43}$$

$$C_{-,-}(<S_x>,<S_y>)=\frac{2}{\hbar}\left[-\langle S_x\rangle-\langle S_y\rangle+\frac{2}{\hbar}\langle S_x\rangle\langle S_y\rangle\right], \tag{44}$$

and

$$C_{+,-}(\langle S_x\rangle,\langle S_y\rangle)=\frac{2}{\hbar}\left[-\langle S_x\rangle+\langle S_y\rangle-\frac{2}{\hbar}\langle S_x\rangle\langle S_y\rangle\right]. \tag{45}$$

Using Eqs. (35)-(38), the inequality (41) can be recast as follows

$$\begin{aligned}&|\psi_P(2n\pi)|^2\left|\psi_P\left((2n+1)\frac{\pi}{2}\right)\right|^2\log_2\left(|\psi_P(2n\pi)|^2\left|\psi_P\left((2n+1)\frac{\pi}{2}\right)\right|^2\right)\\ &+|\psi_P(2n\pi)|^2\left|\psi_P\left((2n+1)\frac{3\pi}{2}\right)\right|^2\\ &\log_2\left(|\psi_P(2n\pi)|^2\left|\psi_P\left((2n+1)\frac{3\pi}{2}\right)\right|^2\right)\\ &+|\psi_P((2n+1)\pi)|^2\left|\psi_P\left((2n+1)\frac{\pi}{2}\right)\right|^2\\ &\log_2\left(|\psi_P((2n+1)\pi)|^2\left|\psi_P\left((2n+1)\frac{\pi}{2}\right)\right|^2\right)\\ &+|\psi_P((2n+1)\pi)|^2\left|\psi_P((2n+1)\frac{3\pi}{2})\right|^2\log_2(|\psi_P((2n+1)\pi)|^2\\ &\left|\psi_P\left((2n+1)\frac{3\pi}{2}\right)\right|^2\right)\le 4.\end{aligned} \tag{46}$$

2.4. The Shannon entropy for multi-moded structures

Eq. (1) holds for a structure with M propagating modes on either sides of the scattering region. In that case, the (a^+,b^-) incoming and (b^+,a^-) outgoing wave amplitudes are column vectors of size $(M\times 1)$ and the r,r',t,t' are $M\times M$ square matrices. If the electron is incident from the i th mode in the left contact of the interferometer in Fig. 3, and the leads and branches have M propagating modes, it can be easily shown that the wave intensity at point P next to the right lead is given by

$$|\psi_P|^2 = 1+\sum_j r_{ji}^* t_{ji} e^{i(k_j^u-k_j^l)L}+\sum_j t_{ji}^* r_{ji} e^{-i(k_j^u-k_j^l)L}, \tag{47}$$

where the r_{ji}'s and t_{ji}'s are the reflection and transmission amplitudes into mode j for a mode incident in channel i. The quantities k_j^u's and k_j^l's are the wavevectors associated with mode j in the upper and lower arm of the ring, respectively. If we independently adjust the gate potentials in both arms to make $k_j^u=k_j^l$, then we get

$$|\psi_P|^2 = 1+\frac{2}{\hbar}\langle S_x^i\rangle, \tag{48}$$

where

$$S_x^i=\hbar\, Re\left(\sum_j r_{ji}^* t_{ji}\right), \tag{49}$$

which we write in the more compact form

$$S_x^i=\hbar\, Re(r_i^\dagger t_i), \tag{50}$$

where $r_i^\dagger$ is the $(1\times M)$ row vector

$$r_i^\dagger=(r_{1i}^*, r_{2i}^*,\ldots,r_{Mi}^*), \tag{51}$$

and t_i is the $(M\times 1)$ column vector

$$t_i=(t_{1i},t_{2i},\ldots,t_{Mi})^\top, \tag{52}$$

where $\top$ stands for the transpose operation.

By analogy, extending Eq. (9) to the multi-moded case, we introduce the other two effective spin components for the i th propagating mode,

$$S_y^i=-\hbar\,\mathrm{Im}(r_i^\dagger t_i)=-\hbar\,\mathrm{Im}\left(\sum_j r_{ji}^* t_{ji}\right) \tag{53}$$

and

$$S_z^i=\frac{\hbar}{2}\left(2\sum_j|t_{ji}|2-1\right). \tag{54}$$

The coefficients r_{ji} and t_{ji} satisfy the following relations:

$$\sum_j(|t_{ji}|^2+|r_{ji}|^2)=1, \tag{55}$$

for $i=1,2,\ldots,M$.

Using the Cauchy-Schwartz's inequality, it was shown in Ref. [6]

$$S_x^{i2}+S_y^{i2}+S_z^{i2}\le\frac{\hbar^2}{4}. \tag{56}$$

By introducing the vector $\vec{v}_i$ with the three components

$$\vec{v}_i = \frac{2}{\hbar}(S_x^i, S_y^i, S_z^i) \tag{57}$$

we find that the inequality (56) simply states that $\vec{v}_i$ is a vector within the Bloch ball, i.e., the interior of the Bloch sphere. This formalism is equivalent to a density matrix description for each mode by a two-dimensional density matrix given by

$$\rho_i = \tfrac{1}{2}(I + \vec{v}_i.\vec{\sigma}), \tag{58}$$

where each channel is described as a mixed-state because of the coupling between modes inside the device.

In the next section, we use the *effective spin* formalism to revisit the problem of coherent charge transport through an array of two-dimensional elastic scatterers from a quantum information perspective. We calculate the length dependence of the Shannon entropy $\overline{H}$ (averaged over a large number of samples), its variance ΔH, and the signal to noise ratio $\overline{H}/\Delta H$, starting with the definition

$$H = \sum_i H_i = -\sum_i [|r_i|^2 \log_2 |r_i|^2 + |t_i|^2 \log_2 |t_i|^2], \tag{59}$$

where $|r_i|^2 = \sum_j |r_{ji}|^2$ and $|t_i|^2 = \sum_j |t_{ji}|^2$.

Finally, we define cross-correlation coefficients

$$\Gamma_a(i,j) = \Gamma_a(j,i) = \overline{S_a^i S_a^j} - \overline{S_a^i}.\overline{S_a^j}, \tag{60}$$

where $a = x$, y, or z and the indices i and j vary from 1 to M.

Performing a double summation over i and j (with $i \neq j$) and also summing over x, y, and z, we get

$$H_{eff} = H_{eff}^{\perp} + H_{eff}^{\parallel}, \tag{61}$$

where

$$H_{eff}^{\perp} = \sum_i \sum_{j(j\neq i)} [\Gamma_{xx}(i,j) + \Gamma_{yy}(i,j)], \tag{62}$$

and

$$H_{eff}^{\parallel} = \sum_i \sum_{j(j\neq i)} \Gamma_{zz}(i,j). \tag{63}$$

H_{eff} can also be written explicitly as follows:

$$H_{eff} = \sum_i \sum_{j(j\neq i)} \overline{\vec{S}^i}.\overline{\vec{S}^j} - \sum_i \overline{\vec{S}^i}.\vec{b}_{eff}^{\,i}, \tag{64}$$

with

$$\overline{\vec{S}}^i = (\overline{S_x^i}, \overline{S_y^i}, \overline{S_z^i}) \tag{65}$$

and

$$\vec{b}_{eff}^{\,i} = \sum_{j(j\neq i)} \overline{\vec{S}}^j. \tag{66}$$

The quantity H_{eff} can be interpreted as the sum of two terms: (a) $\sum_i \sum_{j(j\neq i)} \vec{S}^i.\vec{S}^j$ is an effective Heisenberg Hamiltonian with a common exchange interaction between the effective spins and (b) $-\sum_i \vec{S}^i.\vec{b}_i$ is similar to the Zeeman interaction for the i th effective spin in the effective magnetic field $\vec{b}_i$ generated by the other effective spin components. As will be shown in the numerical simulations in the next section, the quantity H_{eff} reaches a minimum for sample length equal to the elastic mean-free path.

3. Numerical examples

Transport through random arrays of delta scatterers: (a) *Single-moded structures (one propagating mode—zero evanescent state):* We first consider a random array of delta-scatterers of strength $V_I\delta(x-(x_0^i+(i-1)a)$, where V_I is selected to be 0.3 eV Å and x_0^i is the location of the i th impurity located in the interval $[(i-1)a, ia]$. Each impurity location is generated using a uniform random number in each interval. The length of each subsection is set equal to 237 Å and the wavevector of the incident electron $k = \sqrt{2m^*E_F}/\hbar$, is selected such that $ka = \pi$, for an incident energy E_F of 10 meV and $m^* = 0.067m_0$, the electron effective mass in GaAs.

While averaging over 10^5 samples, it was found in Ref. [6] that the average conductance reaches a value of e^2/h for an elastic mean free path equal to 23×237 Å ~ 0.55 μm. In Fig. 4, we illustrate the validity of the inequalities (31) and (33) for a specific sample. The following features appear: (a) the Shannon entropy is a rapidly fluctuating function of the sample length. For instance, close to $N = 20$, H_{bin}^{QM} varies abruptly from nearly 0 to its maximum value of 1. (b) The functions $g(\langle S_x\rangle)$ and $g(\langle S_y\rangle)$ are quite different in the regime extending from the ballistic regime to sample length equal to a few times the elastic mean free path. (c) H_{bin}^{QM} nearly coincides with either $g(\langle S_x\rangle)$ or $g(\langle S_y\rangle)$ for specific

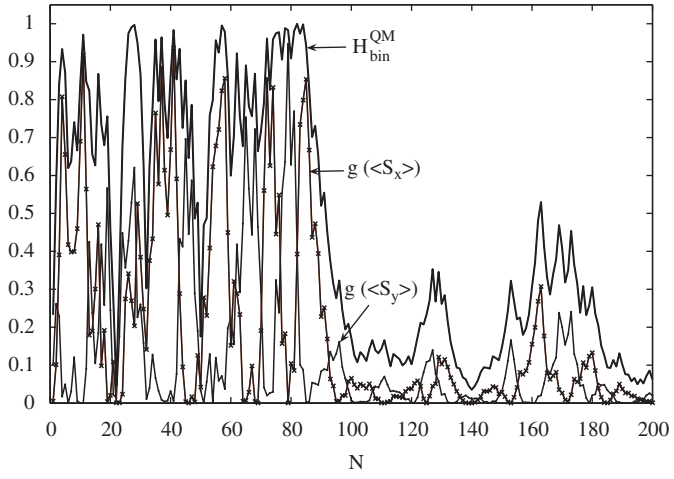

Fig. 4. Plot of the quantities $g(\langle S_x\rangle)$ and $g(\langle S_y\rangle)$ and the Shannon binary entropy H_{bin}^{QM} as a function of the number of impurities crossed for a specific array of one-dimensional delta-scatterers.

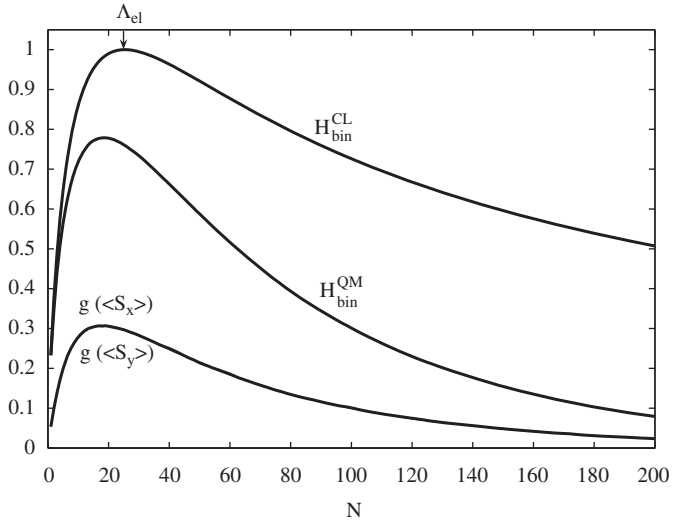

Fig. 5. Plot as a function of sample length of the average (over an ensemble of 10^5 samples of one-dimensional delta-scatterers) of the quantities $g(\langle S_x\rangle)$ and $g(\langle S_y\rangle)$. Also shown are the average values of the classical $H_{bin}^{CL}(|t|^2)$ and quantum-mechanical $H_{bin}^{QM}(|t|^2)$ binary entropies.

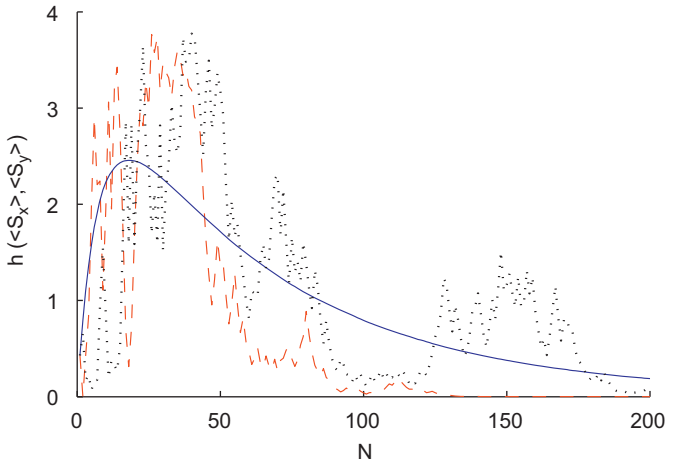

Fig. 6. Plot as a function of sample length of the value of the function $h(\langle S_x\rangle, \langle S_y\rangle)$ in Eq. (41) for two specific impurity configurations (shown as dashed and dotted lines). Also shown as a full line is the average of $h(\langle S_x\rangle, \langle S_y\rangle)$ taken over an ensemble of 10^5 impurity configurations.

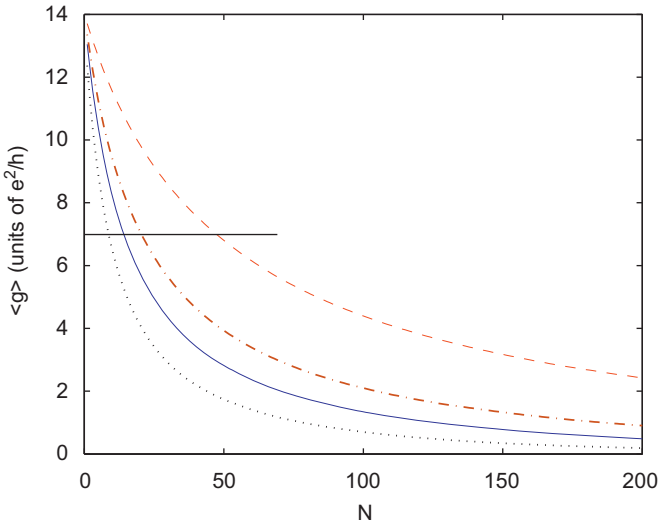

Fig. 7. Plot of the sample length dependence of the average over 10^4 samples of the conductance (in units of e^2/h). The dashed and dotted lines correspond to the case of repulsive and attractive scatterers. The full line is for samples containing half-attractive and half-repulsive impurities. The dot–dash line corresponds to the average calculated using seven propagating modes only with samples containing half-attractive and half-repulsive impurities.

sample lengths. (d) H_{bin}^{QM} is substantially smaller than unity for sample length well into the strong localization regime.

Fig. 5 illustrates the validity of the inequalities (31) and (33) after averaging both sides over 10^5 arrays. In that case, the average values of $g(\langle S_x\rangle)$ and $g(\langle S_y\rangle)$ are virtually equal. Also shown in Fig. 5 are the binary entropies calculated after cascading either probability H_{bin}^{CL} or amplitude H_{bin}^{QM} scattering matrices; H_{bin}^{QM} includes the effects of multiple reflections between scatterers, whereas H_{bin}^{CL} does not. The latter does not vary much from sample to sample and reaches a maximum value of 1 for $N=\Lambda_{el}$. On the other hand, H_{bin}^{QM} (averaged over many samples) peaks for sample length slightly below the elastic mean free path and its maximum value is below 0.8. Furthermore, H_{bin}^{QM} is substantially below H_{bin}^{CL} for sample length deeply into the strong localization regime, i.e., for $N>\Lambda_{el}=\Lambda_{loc}$.

Finally, Fig. 6 is a plot of inequality (41) where the function $h(<S_x>, <S_y>)$ was calculated for two specific samples (broken lines). The inequality (41) is nearly an equality at some specific value of the sample length. Also shown (solid line) is the value of $h(<S_x>, <S_y>)$ after averaging over an ensemble of 10^5 arrays.

(b) *Multi-moded structures*: We used the scattering-matrix formalism outlined in Refs. [11,12] to calculate the reflection and transmission amplitudes as a function of sample length of an ensemble of two-dimensional random arrays of delta-scatterers. The direction of propagation of the current is along the x-axis and a particle-in-a-box model is used along the width of the wire (y-axis). Along the x-axis, the impurities are separated evenly and located halfway in each segment of length $a=200\,\text{Å}$. In the y-direction, a uniform probability distribution is used across the width of the wire $y=2500\,\text{Å}$. The effective mass in the channel is assumed to be $m^*=0.067m_0$ which corresponds to a GaAs channel. The scattering potential of each impurity is given by

$$V_{imp}(x,y)=V_I\delta(x-x_i)\delta(y-y_i), \tag{67}$$

with $V_I=\pm 200\,\text{eV Å}^2$ i.e., either repulsive (positive V_I) or attractive (negative V_I) scatterers, and (x_i,y_i) are the coordinates of the i th impurity as described above.

Despite the fact that they do not carry any current, evanescent modes can have a very profound effect on the calculation of the conductance in mesoscopic systems since they can renormalize the transmission and reflection coefficients associated with the current-carrying propagating modes [7–10]. Hereafter, we analyze the influence of propagating modes on the Shannon entropy content of two-dimensional random arrays of elastic scatterers. All physical quantities were calculated as averages (quantities indicated with a horizontal bar) over 10^4 samples. The Fermi level was set equal 1 meV above M^2E_1 (with $M=7$), the threshold of the seventh lowest free propagating mode in the channel. E_1 is the energy threshold for free propagation in the lowest mode, i.e., $E_1=\pi^2\hbar^2/2m^*W^2=90\,\mu\text{eV}$.

Fig. 7 is a plot of the conductance versus number of scatterers crossed in the channel for samples with either repulsive, or attractive scatterers, or a 50%–50% mixture of both types. The simulations included the seven lowest evanescent states in the channel. We have checked that all the results discussed hereafter did not change much when additional evanescent modes were included in the simulations. The elastic mean-free path was estimated by finding the closest integer (number of scatterers crossed) for which the conductance is reduced to $M/2$ (in units of e^2/h). The actual mean free path is then obtained by multiplying this number by the quantity $a(=200\,\text{Å})$, which is the size of each subsection containing a single scatterer along the x-direction. From Fig. 7, the elastic mean-free path Λ_{el} is found equal to 9, 14, and 47, for samples with all attractive, half attractive-half repulsive, and all repulsive scatterers, respectively. The dot–dash line shows the result obtained for samples with half attractive-half repulsive scatterers when only the seven propagating modes are included in the simulations. These results stress the importance of including the effect of the evanescent modes when calculating the transmission amplitudes t_{ij}'s of the propagating modes [7–10]. The variance of the conductance for the samples described above is plotted in Fig. 8. Interestingly, the universality of the conductance fluctuations, i.e., a constant value for Δg in the weak localization regime (samples with length between the elastic mean free path Λ_{el} and the localization length $\Lambda_{loc}=M\Lambda_{el}$) *is only valid for samples with repulsive scatterers*. In contrast, if we exclude the evanescent states, then both the conductance and its variance become nearly independent of the nature of the scatterer potential and the universality of the conductance fluctuations is

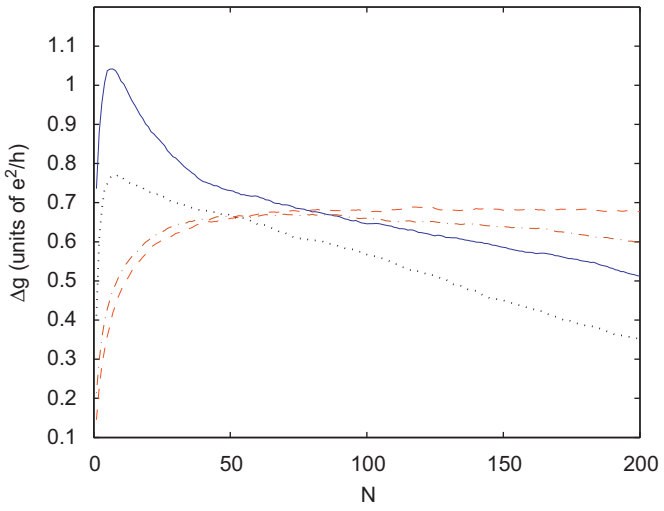

Fig. 8. Variance of the conductance fluctuations (in units of e^2/h) versus number of scatterers crossed. The dashed and full lines correspond to the case of repulsive and attractive scatterers. The full line is for samples containing half-attractive and half-repulsive scatterers. The dot–dash line corresponds to the average calculated using seven propagating modes only with samples containing half-attractive and half-repulsive scatterers.

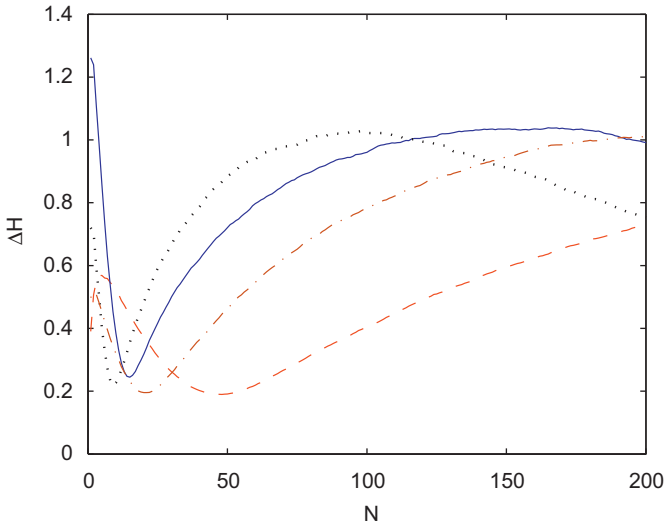

Fig. 10. Variance of the Shannon entropy versus number of scatterers crossed. The dashed and full lines correspond to the case of repulsive and attractive scatterers. The full line is for samples containing half-attractive and half-repulsive scatterers. The dot–dash line corresponds to the average calculated using seven propagating modes only with samples containing half-attractive and half-repulsive scatterers.

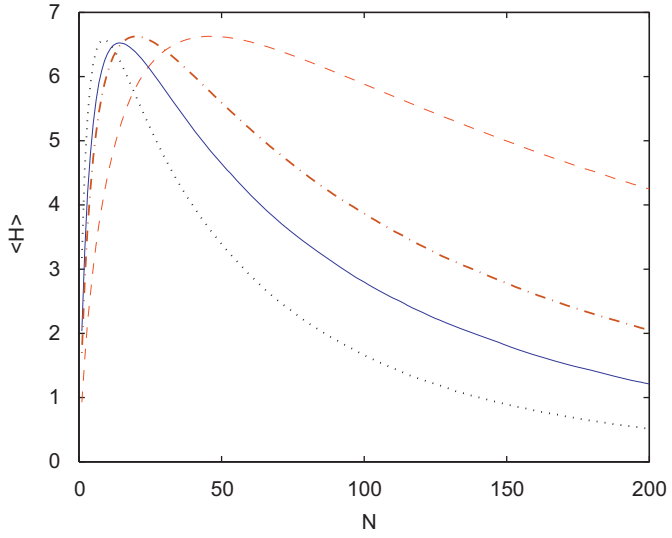

Fig. 9. Plot of the average over 10^4 samples of the Shannon entropy versus number of scatterers crossed. The dashed and full lines correspond to the case of repulsive and attractive scatterers. The full line is for samples containing half-attractive and half-repulsive scatterers. The dot–dash line corresponds to the average calculated using seven propagating modes only with samples containing half-attractive and half-repulsive scatterers.

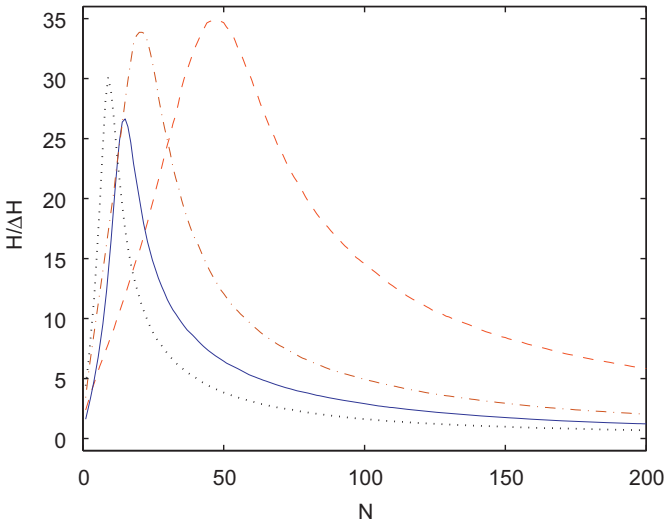

Fig. 11. Plot of the signal-to-noise ratio $\mathrm{SNR} = \langle H \rangle / \Delta H$ versus number of scatterers crossed. The dashed and full lines correspond to the case of repulsive and attractive scatterers. The full line is for samples containing half-attractive and half-repulsive scatterers. The dot–dash line corresponds to the average calculated using seven propagating modes only with samples containing half-attractive and half-repulsive scatterers.

upheld for all types of scatterers – both attractive and repulsive. We speculate that this is due to the fact that in the case of attractive scatterers, bound states form, which interact with evanescent modes and change the nature of transport in a very non-trivial way. Therefore, these simulations highlight the importance of evanescent modes.

Fig. 9 is a plot of the average of the Shannon entropy versus length for the samples described above. The maximum of the average Shannon entropy occurs slightly below $M = 7$, the number of propagating modes in the samples. We expect this to happen if we cascade probability scattering matrices instead of amplitude scattering matrices. One effect of the quantum interferences is to lower the value of the maximum Shannon entropy of arrays of elastic scatterers. The maximum always occurs when the sample length is equal to the electron mean free path, and its value is virtually independent of the nature of the scatterers. As shown in Fig. 9, it is found that, past its peak, the Shannon entropy is substantially larger for samples containing repulsive scatterers than for sample containing attractive scatterers.

Fig. 10 is a plot of the variance of the Shannon entropy versus number of scatterers crossed. It reaches a minimum at a value equal to the elastic mean free path. The minimum in ΔH, ~ 0.2, is nearly independent of the nature of the scatterers and about equal to the value obtained for $\Delta H_{\min}$ for the case when there is only one propagating mode in the channel [6]. Furthermore, in the weak localization regime, i.e., for samples with number of scatterers in the range $\Lambda_{el} < N < \Lambda_{loc} = M\Lambda_{el}$, the value of

ΔH is not universal. For $N > 50$, i.e., in the weak localization regime, ΔH is the lowest for the case of samples with repulsive scatterers.

When considering arrays of elastic scatterers as quantum information processors, it would be best to use samples with length for which the signal to noise ratio, SNR $= \langle H \rangle / \Delta H$ reaches a maximum. Using the results from Figs. 9 and 10, we plot in Fig. 11 the length dependence of the SNR for the various samples considered above. This figure indicates that SNR reaches a maximum for sample length equal to the electron mean free path independent of the nature of the scatterers. The highest peak is obtained for a sample with repulsive scatterers and the lowest peak value is obtained for sample containing a 50%–50% ratio of repulsive and attractive scatterers.

Fig. 12 is a plot of the ratio of the signal to noise ratios calculated for samples with repulsive scatterers SNR_R compared to samples with attractive scatterers SNR_A. The ratio SNR_R/SNR_A drops from a factor 10 for sample length equal to the elastic mean free path for arrays with repulsive scatterers (i.e., $\Lambda_{el} \sim 47$). Therefore, as quantum information processors, there is a larger window of tunability of the SNR of the Shannon entropy for samples with attractive scatterers if surrounding gates can be used to tune the nature of the impurity potential from repulsive to attractive by moving their energy states around the quasi-Fermi level throughout the sample. Fig. 12 also shows that for $N > \Lambda_{el} \sim 47$, i.e., in the weak localization regime, the ratio SNR_R/SNR_A is virtually independent of the sample length.

Next, we plot the length dependence of the cross-correlations coefficients defined in Eq. (60). The sample width was kept at 2500 Å and the Fermi level was set 0.3 meV above $9E_1 = 0.81$ meV, the threshold energy for three propagating modes in the channel. The length dependence of the average over 10^4 samples for $\Gamma_{xx}(i,j)$, $\Gamma_{yy}(i,j)$, and $\Gamma_{zz}(i,j)$, is shown in Figs. 13, 14, and 15, respectively. The scatterers were assumed to be 100% repulsive and only propagating modes were considered in the simulations. A plot of the average conductance versus number of scatterers crossed reveal an elastic mean free path of 10 for these samples. The individual cross-correlation coefficients have either positive or negative values depending on the indices (i,j). As shown in Figs. 13, 14, and 15, the cross-correlation coefficients $\Gamma_{aa}(1,3)$, $\Gamma_{aa}(2,3)$ for $a = x$, y, and z are nearly

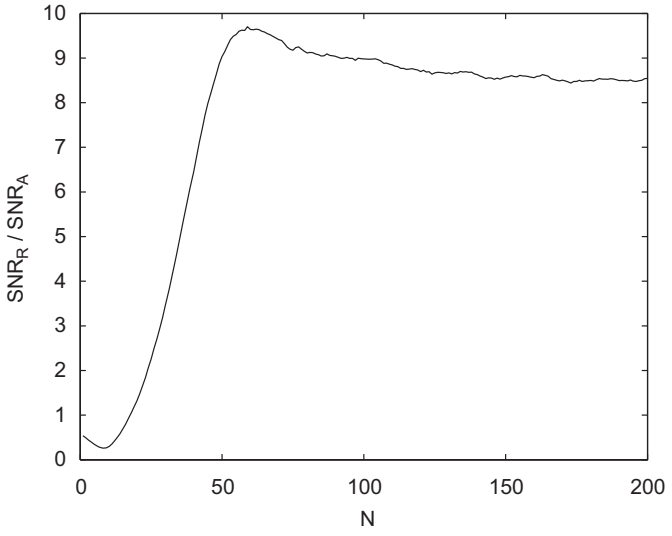

Fig. 12. Plot of the ratio SNR_R/SNR_A versus number of scatterers crossed, where SNR_R and SNR_A are the signal to noise ratio for the Shannon entropy calculated for samples with repulsive and attractive scatterers, respectively.

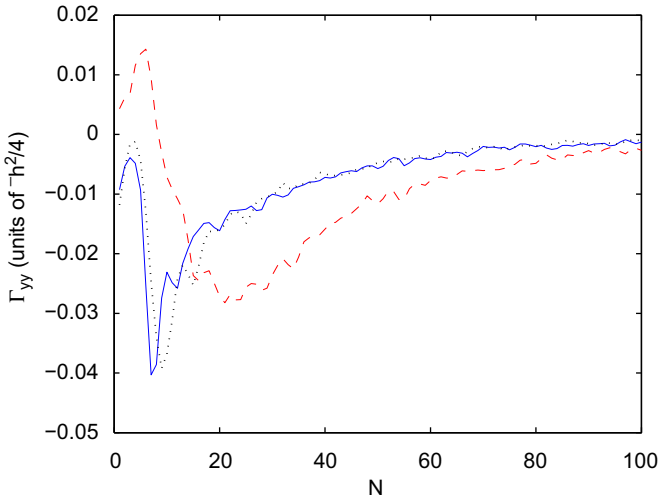

Fig. 14. Plot of the average over 10^4 samples of $\Gamma_{yy}(1,2)$ (dashed line), $\Gamma_{yy}(1,3)$ (full line), and $\Gamma_{yy}(2,3)$ (dotted line), versus the number of scatterers crossed.

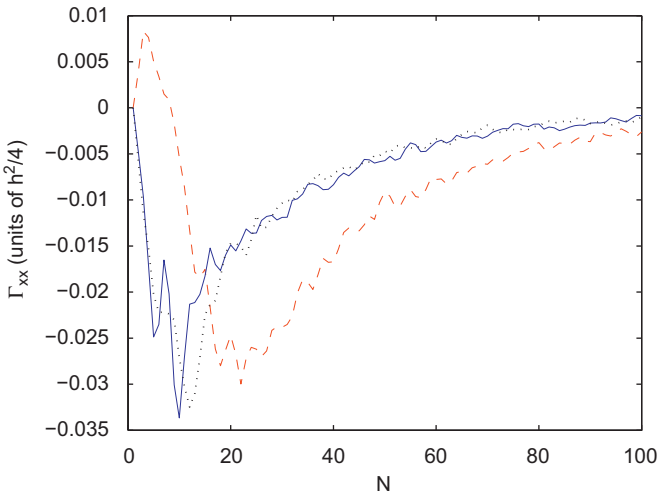

Fig. 13. Plot of the average over 10^4 samples of $\Gamma_{xx}(1,2)$ (dashed line), $\Gamma_{xx}(1,3)$ (full line), and $\Gamma_{xx}(2,3)$ (dotted line), versus the number of scatterers crossed.

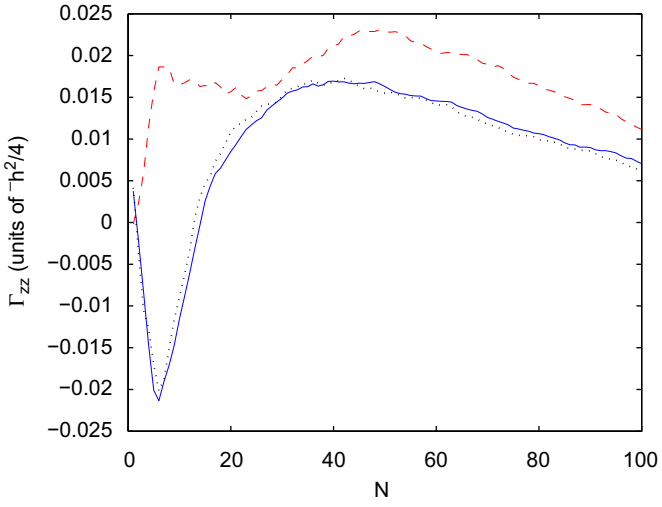

Fig. 15. Plot of the average over 10^4 samples of $\Gamma_{zz}(1,2)$ (dashed line), $\Gamma_{zz}(1,3)$ (full line), and $\Gamma_{zz}(2,3)$ (dotted line), versus the number of scatterers crossed.

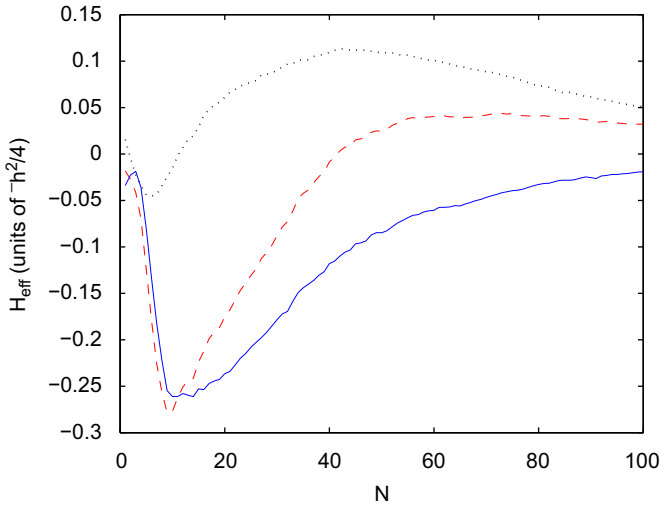

Fig. 16. Plot of the average over 10^4 samples of $H_{eff}^{\perp}$ (full line), $H_{eff}^{\parallel}$ (dotted line), and $H_{eff} = H_{eff}^{\perp} + H_{eff}^{\parallel}$ (dashed line), versus the number of impurities crossed. H_{eff} reaches a minimum for sample length equal to the elastic mean free path ($N = 10$).

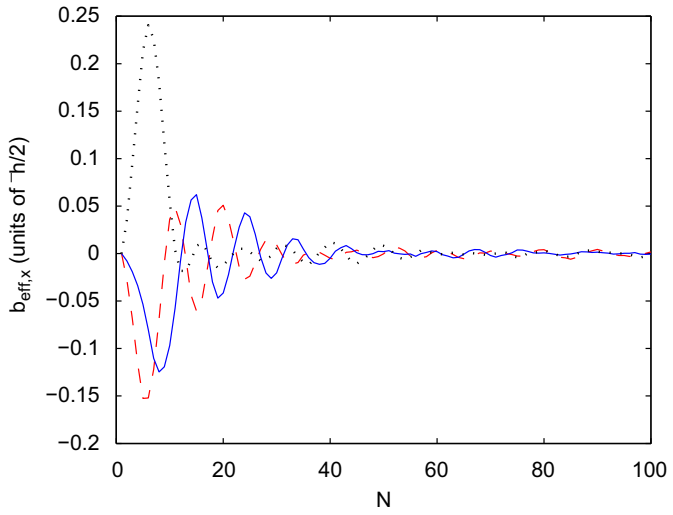

Fig. 17. Plot of length dependence of the x-component of the effective magnetic field $b_{eff,x}$ associated with the three lowest propagating modes. The dashed, full, and dotted lines correspond to modes 1, 2, and 3, respectively.

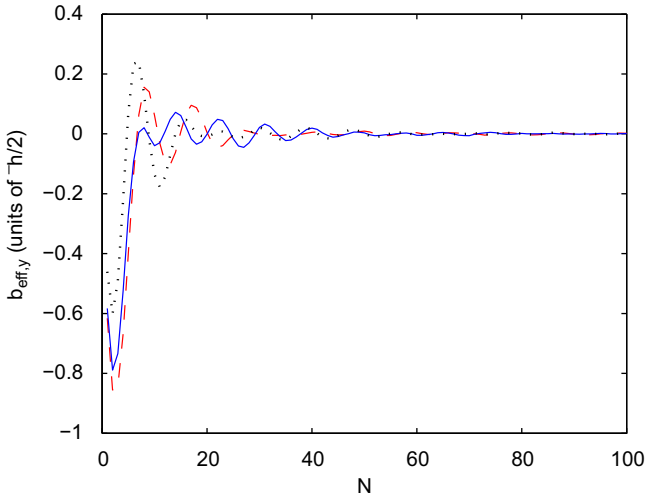

Fig. 18. Plot of length dependence of the y-component of the effective magnetic field $b_{eff,y}$ associated with the three lowest propagating modes. The dashed, full, and dotted lines correspond to modes 1, 2, and 3, respectively.

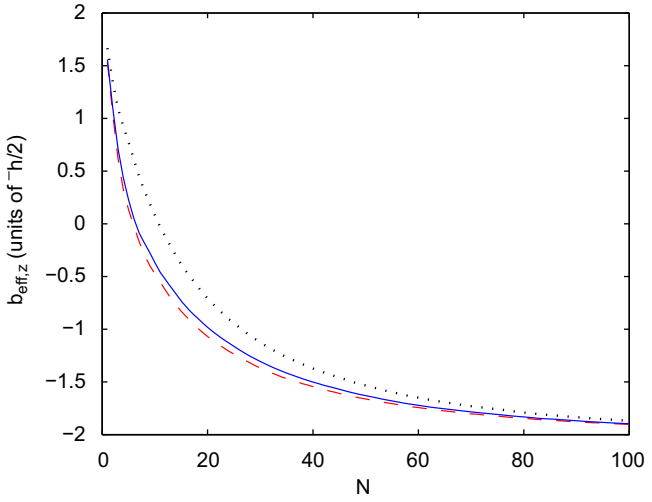

Fig. 19. Plot of length dependence of the z-component of the effective magnetic field $b_{eff,z}$ associated to the three lowest propagating modes. The dashed, full, and dotted line corresponds to mode 1, 2, and 3, respectively.

identical and markedly different from $\Gamma_{aa}(1,3)$. These specific features require further investigation, but are obviously related to the number of nodes in the transverse part of the wavefunction associated with each propagating channel. These transverse wavefunctions control the amount of overlap between subbands in the wire and hence the amount of correlations between the transmission and reflection coefficients.

Next, we focus on a global property of the cross-correlation coefficients by summing them with equal weight over the indices i and j (with $i \neq j$), a quantity which we called H_{eff}. The latter was found to reach a minimum at the value of the elastic mean-free path, as shown in Fig. 16. This specific feature was also found when considering samples with different ratios of repulsive and attractive impurities and with different number of propagating modes in the channel. Also shown in Fig. 16 as full and dotted lines are the contributions to $H_{eff}^{\perp}$ and $H_{eff}^{\parallel}$, as defined in Eqs. (62) and (63), respectively. The contribution to $H_{eff}^{\parallel}$ which characterizes the correlation of the effective spin components in the equatorial plane of the Bloch sphere is always negative. This means that the projections in the equatorial plane of the average of the effective spin components make an angle larger than 90°. $H_{eff}^{\perp}$, on the other hand, is mostly positive because the average of the projections of the effective spin z-components gradually move from the North pole to the South pole as the sample length increases.

Finally, the length dependence of the x, y, and z components of the effective magnetic field defined in Eq. (66) and acting on the effective spinors associated with the propagating modes are shown in Figs. 17, 18, and 19, respectively. For all three effective spins, $b_{eff,z}$ start with a maximum value of 2 (in units of $\hbar/2$) in the ballistic regime, as all effective spins are at the North pole on the Bloch sphere. As the length of the sample increases, all $b_{eff,z}$'s smoothly decay to a minimum value of -2 (in units of $\hbar/2$) as all three effective spins eventually reach the South pole as the sample length goes far into the strong localization regime. The x and y components of the effective magnetic field start both from zero in the ballistic regime as the effective spins are at the North pole. The amplitudes of $b_{eff,x}$ and $b_{eff,y}$ are the largest for sample length below the elastic mean free path as the effective spins spiral down around the z axis of the

Bloch sphere as they penetrate into the Bloch ball towards the equatorial plane. These oscillations in $b_{eff,x}$ and $b_{eff,y}$ quickly die out for sample length in the weak localization regime and are virtually zero once into the strong localization regime. Therefore, the plots in Figs. 17, 18 and 19 show the richness in the behavior of the cross-correlation coefficients as we vary the sample length from the ballistic regime to a few times the elastic mean free path.

4. Conclusions

Using an *effective spin* concept, we have examined the potential use of random arrays of elastic scatterers as quantum information processors by calculating the properties of their Shannon entropy $H_{bin}(|t|^2)$ assuming phase coherent charge transport. A lower bound for $H_{bin}(|t|^2)$ is found starting with the entropic quantum uncertainty principle. Evanescent modes strongly affect the Shannon entropy and its associated signal-to-noise ratio (SNR). The numerical values for these quantities are strongly sensitive to the nature of the scatterers, i.e., whether they are attractive, repulsive, or a combination of both. As quantum information processors, there is a large window of tunability of the SNR of the Shannon entropy for samples with repulsive scatterers if the action of surrounding gates can be used to change the scattering potential from repulsive to attractive by moving their energy levels with respect to the quasi-Fermi level throughout the sample. It is found that the mean free path of random array of elastic scatterers is the length scale at which the sum of the cross-correlations coefficients of the effective spin components reaches a minimum. This result can be interpreted as a minimum energy state for the sum of effective Heisenberg and Zeeman Hamiltonians associated with the effective spins describing the propagating channels in the transport problem.

Since H_{eff} can be written as sum of a terms resembling three-dimensional Heisenberg and Zeeman Hamiltonians as shown in Eq. (64), the numerical simulations reported here suggest an unexpected connection between phase transition phenomena and coherent charge transport through arrays of random scatterers. This analogy would need to be explored in further detail.

Even though the analysis of this paper is based on the effective spin concept for electron waves, the latter can be readily extended to the analysis of the propagation of radiofrequency signals in microwave cavities, or photons through optical waveguides. In the latter, the arrays of elastic scatterers considered in this paper could be replaced by such entities as photonic crystals [21].

References

[1] C.H. Holbrow, E.J. Galvez, M.E. Parks, Amer. J. Phys. 70 (2002) 260.
[2] T.B. Pittman, B.C. Jacobs, J.D. Franson, Phys. Rev. A 64 (2001) 062311.
[3] P.T. Cochrane, G.J. Milburn, Phys. Rev. A. 64 (2001) 062312.
[4] I. Neder, N. Ofek, Y. Chung, M. Heiblum, D. Mahalu, V. Umansky, Nature 448 (2007) 333 and see references therein.
[5] P. Samuelson, I. Neder, M. Büttiker, Phys. Rev. Lett. 102 (2009) 1062804.
[6] J. Wan, W. Liu, M. Cahay, V. Gasparian, S. Bandyopadhyay, The effective spin concept to analyze coherent charge transport in mesoscopic systems, arXiv:0909.2892v1.
[7] P.F. Bagwell, Phys. Rev. B 41 (1990) 10354.
[8] M. Cahay, S. Bandyopadhyay, M.A. Osman, H.L. Grubin, Surf. Sci. 228 (1990) 301.
[9] S. Bandyopadhyay, M. Cahay, D. Berman, B. Nayfeh, Superlattices and Microstructures 10 (1991) 327.
[10] J. Heinrichs, Phys. Rev. B 68 (2003) 155403.
[11] S. Datta, M. Cahay, M. McLennan, Phys. Rev. B 36 (1987) 5655.
[12] M. Cahay, M. McLennan, S. Datta, Phys. Rev. B 37 (1988) 10125.
[13] M.A. Nielsen, I.L. Chuang, Quantum Computation and Quantum Information, Cambridge University Press, NY, 2000.
[14] S. Bandyopadhyay, M. Cahay, Introduction to Spintronics, CRC Press, Boca Raton, 2008.
[15] Using the unitary property of the scattering matrix, it can be easily checked that the trace of the matrix ρ is unity and ρ satisfies the following properties: $\rho^{\dagger}=\rho$, $\rho^2=\rho$, and $Tr[\rho^2]=Tr[\rho]=1$, which are all characteristic of the density matrix associated with a pure state [13].
[16] Y.M. Blanter, M. Büttiker, Phys. Rep. 336 (2000) 1.
[17] R. Landauer, IBM J. Res. Dev. 1 (1957) 223.
[18] Y. Imry, Introduction to Mesoscopic Physics, Oxford University Press, Oxford, 2002.
[19] C.W.J. Beenakker, H. van Houten, in: H. Ehrenreich, D. Turnbull (Eds.), Solid State Physics, vol. 44, Academic Press, Boston, 1991, p. 1.
[20] M. Cahay, S. Bandyopadhyay, in: P.W. Hawkes (Ed.), Advances in Electronics and Electron Physics, vol. 89, Academic Press, San Diego, 1994, p. 94.
[21] J.D. Joannopoulos, S.G. Johnson, J.W. Winn, R.D. Meade, Photonic Crystals: Molding the Flow of Light, Princeton University Press, Princeton, 2008.